JOURNAL OF CATALYSIS 127, 553–575 (1991)

Kinetics and Multiple Rate States of CO Oxidation on Pt

II. Linking UHV and Atmospheric Pressure Kinetic Behavior

MICHAEL P. HAROLD* AND MARTHA E. GARSKE

Department of Chemical Engineering, University of Massachusetts, Amherst, Massachusetts 01003

Received December 28, 1989; revised September 19, 1990

In this second part of a two-part study, two new kinetic models developed in the first part (Harold and Garske (*1*)) are used to simulate Pt-catalyzed CO oxidation over a wide range of catalyst temperatures, gas compositions, and total pressures. The models are modifications of the commonly used three-step sequence (model I). Model II contains steps involving adsorbed molecular oxygen, and reaction steps between gas phase CO and adsorbed oxygen species. In model III an oxygen site exclusion feature replaces the two Eley–Rideal steps. A comparison of model predictions and experimental data obtained at pressures spanning UHV and atmospheric provides for sensitive discrimination between the models. The models are used to simulate multivalued UHV Pt(110)-catalyzed CO oxidation rate data (Sung (*2*)). Kinetic parameters are estimated using a novel nonlinear regression scheme involving both singular and nonsingular data. Models II and III simulate the data equally well. Agreement is good between model II and III predictions and the intermediate pressure data for Pt(100) (Berlowitz *et al.* (*3*)), and for polycrystalline Pt (Garske and Harold (*4, 5*)) using the estimated parameters from the UHV data simulation. Intrinsic rate multiplicity is predicted to persist at these pressures over a narrow range of temperature and gas composition. External mass transport resistance is incorporated into model II to simulate atmospheric pressure CO oxidation experiments. The predicted range of conditions giving multiplicity expands considerably. Several atmospheric pressure experimental trends are predicted, such as the upright cusp shape of the temperature–CO pressure bifurcation map for low CO/O_2 observed in many studies, and the sharp transition in the extinction branch at the stoichiometric ratio observed by Kaul *et al.* (*6*). The latter trend is shown to occur for a class of much simpler single-valued kinetic models. The simulations of CO oxidation over a wide pressure range are shown to provide insight about bridging the gap between surface science and realistic operating conditions.

INTRODUCTION

The kinetics of CO oxidation on unsupported and supported noble metal catalysts are quite complex despite the seemingly straightforward mechanism. Many experimental and modeling studies have been undertaken to better understand the reaction. Extensive reviews are provided by Engel and Ertl (*7*) and Razon and Schmitz (*8*). The basic qualitative kinetic features of isothermal Pt-catalyzed CO oxidation under conditions of negligible transport limitations are quite consistent for many catalyst types. These trends, some of which were discussed in the first part (*1*), are now summarized.

For low values of the $CO–O_2$ ratio (p_{CO}/p_{O_2}) the following behavior has been observed:

(i) Reaction order with respect to CO usually unity but values up to 4 have been reported (*2*).

(ii) Reaction order with respect to oxygen between 0 and 1.

(iii) A temperature-insensitive rate (apparent activation energy approaching zero).

For high p_{CO}/p_{O_2} the following trends have been observed:

(iv) Reaction order with respect to CO of (-1). Some studies reveal a shift to zero order at sufficiently low temperatures (*9, 3*).

(v) Reaction order with respect to oxygen of unity.

(vi) Apparent activation energy approxi-

* To whom correspondence should be addressed.

0021-9517/91 $3.00

mately equal to the CO binding energy (about 30 kcal/mol). Some studies reveal a decrease to about 15 kcal/mol at low temperatures (*9, 3*).

Some studies have reported a multivalued rate at UHV (e.g., (*10, 11, 2*)), conditions for which mass transport limitations are minimal. The observed multiplicity features under transport-limitation-free conditions are:

(vii) Bifurcation diagrams: Clockwise dependence of the rate on CO pressure at a fixed oxygen pressure and catalyst temperature, and a counterclockwise dependence of the rate on temperature for a fixed gas composition. Bifurcation maps: Catalyst temperature–CO pressure bifurcation map in the shape of an inverted cusp, and oxygen pressure–CO pressure map in the shape of an upright cusp.

Reports of isothermal rate multiplicity at higher pressures are much more numerous (*8*). At such pressures, transport limitations play a role. The higher pressure isothermal multiplicity features are:

(viii) Bifurcation diagrams: Same form as for UHV conditions. Bifurcation maps: The oxygen pressure–CO pressure map has the upright cusp shape. Unlike the consistency in the kinetic features, shape of the bifurcation diagrams, and shape of the oxygen pressure–CO pressure map over a wide range of conditions and catalyst types, the temperature–CO pressure bifurcation map features observed at higher pressure do not agree with those of the map obtained at UHV. The higher pressure temperature–CO pressure map is in the form of an upright cusp at low CO/O_2. For higher CO/O_2 and temperatures the ignition and extinction loci merge at a high-temperature cusp. Also, the extinction branch exhibits at sharp rise near the stoichiometric point ($CO/O_2 = 2$).

It is clear that a large number of features must be predicted by any proposed kinetic model. Many models have been proposed that satisfy the basic kinetic or multiplicity features, but not both. Meeting this goal is an essential first step toward our second goal of linking the steady-state CO oxidation kinetics observed under UHV conditions to the kinetics observed at intermediate and atmospheric pressures.

Four models were developed in the first part of this study to satisfy the transport-limitation-free kinetic features (i)–(vii). Each model is a modification of the basic model (I):

$$\begin{aligned} &(1): \quad CO + X \leftrightarrow CO\text{–}X \\ &(2): \quad O_2 + 2X \rightarrow 2O\text{–}X \\ &(3): \quad CO\text{–}X + O\text{–}X \rightarrow CO_2 + 2X \end{aligned} \tag{1}$$

Model I was shown to satisfy the essential multiplicity features ((vii) above). It was ruled out because of its failure to predict the correct kinetics in the limiting regimes of high and low p_{CO}/p_{O_2} ((i)–(vi) above).

Models II and III are comprised of the basic steps (1), (2), and (3) of model I and the following additional three steps involving molecularly adsorbed oxygen:

$$\begin{aligned} &(4): \quad O_2 + X \rightarrow O_2\text{–}X \\ &(5): \quad O_2\text{–}X + X \rightarrow 2O\text{–}X \\ &(6): \quad 2CO\text{–}X + O_2\text{–}X \rightarrow 2CO_2 + 3X \end{aligned} \tag{2}$$

Inclusion of steps (4)–(6) enables the high p_{CO}/p_{O_2} features (iv), (v), and (vi) to be predicted. The difference between models II and III has to do with how the correct kinetic trends at low p_{CO}/p_{O_2} are modeled. Model II consists of two additional steps:

$$\begin{aligned} &(7): \quad CO + O\text{–}X \rightarrow CO_2 + X \\ &(8): \quad CO + O_2\text{–}X \rightarrow CO_2 + O\text{–}X + X \end{aligned} \tag{3}$$

Steps (7) and (8) are reactions between gas phase or weakly adsorbed mobile CO and adsorbed atomic and molecular oxygen, respectively. Model III assumes that adsorbed oxygen excludes a fraction of vacant sites for additional oxygen adsorption. This limits the maximum coverage of oxygen. This feature was proposed by Herz and Marin (*12*) for supported Pt catalysts.

Model IV is comprised of the three basic steps (1)–(3) but assumes site exclusion for

both oxygen (as in model III) and CO. The CO site exclusion enables the high p_{CO}/p_{O_2} features (iv), (v), and (vi) to be correctly predicted.

Model V is similar to model II except that oxygen adsorption proceeds only by the two-step molecular precursor route (steps (4) and (5) above). Further, reversible step (4) is assumed to be at equilibrium. Reaction between adsorbed CO and molecular oxygen occurs by the bimolecular step:

$$(9'): \quad CO\text{–}X + O_2\text{–}X \rightarrow CO_2 + O\text{–}X + X \quad (3')$$

In this study, our simulations are primarily of unsupported Pt catalysts for which complete CO coverage has been confirmed by many investigators (see Engel and Ertl (7)). Also, in the first part model V was shown not to predict the correct limiting kinetic behavior in the CO-covered surface regime. For these reasons, models II and III will be considered in the most detail.

This second part is organized as follows. Models II and III are used to simulate the UHV Pt(110) data of Sung (2) which exhibits rate multiplicity. A parameter estimation scheme involving a model simulation of singular and nonsingular point data is developed to carry out this first step. Using the kinetic parameters estimated from this UHV data simulation, models II and III are then used to simulate intermediate pressure data. The extrapolation of models II and III from UHV to intermediate and atmospheric total pressures enables further discrimination. Finally, atmospheric pressure CO oxidation is simulated with mass transport processes incorporated into model II. This approach enables the impact of mass transport effects to be rationally assessed since the intrinsic rate behavior is known a priori. The reader is referred to the first part of this study for the mathematical formulations of the models (*1*).

ULTRAHIGH VACUUM CO OXIDATION

The kinetics of the elementary steps and the overall CO oxidation reaction have been studied under UHV conditions by many investigators (e.g., (7)). Evidence for multiple rate regimes and periodic phenomena have been most commonly reported for the Pt(100) plane. The work of Ertl and coworkers (*13–16*) has demonstrated that the adsorption-induced surface transformation between the hex and (1 × 1) structures is responsible for oscillations. The mechanism causing rate multiplicity is necessarily different for other crystal planes or polycrystalline catalysts at UHV for which reconstruction—if it occurs—has an insignificant effect on the kinetics. As we have demonstrated in the first part and reinforce in this part, steady-state rate multiplicity and the basic kinetic features are predicted without the need for a surface reconstruction mechanism. An approximate way of incorporating the reconstruction into a uniform surface model is presented below.

In this section the CO oxidation kinetics on Pt(110) reported by Sung (2) are examined in some detail. For some of the operating conditions steady-state rate multiplicity was observed. Models II and III are used to simulate the data. Our approach is to test the ability of both models to predict all of the trends in the multivalued UHV rate data, and to simulate the magnitude of the rate and the location of the multiplicity region reasonably well. In later sections, models II and III are used to simulate data obtained by other investigators for other catalyst types at higher pressures. Discrimination between models II and III is based on their relative predictive capabilities over a wide range of conditions.

UHV CO Oxidation on Pt(110) (Sung (2)): Description of Experimental Results

Sung (2) carried out CO oxidation on Pt(110) under ultrahigh vacuum (UHV) conditions. Mixtures of CO and oxygen were admitted continuously into a chamber containing a thin (0.15 cm thick) Pt(110) disk (1.066 cm diameter). During steady-state operation the chamber was pumped contin-

uously by an ion pump with a capacity of 20 liter/s. The CO, O_2, and CO_2 partial pressures were monitored by a mass spectrometer. The CO_2 pressure above background, Δp_{CO_2}, was measured as a function of CO pressure for various combinations of catalyst temperatures and O_2 pressures. The CO oxidation rate is proportional to Δp_{CO_2}, as shown below.

For sufficiently low temperatures and high oxygen pressures, the rate exhibited two stable states for an intermediate range of CO pressure in the form of a clockwise hysteresis loop. A sufficiently high temperature resulted in a single-valued, monotonically increasing curve or one exhibiting a local maximum. The two steady-state branches forming the hysteresis loop exhibited different temperature and CO pressure dependences. The low CO pressure, higher rate regime exhibited an apparent reaction order with respect to CO of between 1 and 2, with little or no dependence on temperature. The higher CO pressure, lower rate regime exhibited an approximate (−0.5)-order dependence on CO with an apparent activation energy between 23 and 33 kcal/mol.

In order to simulate the UHV data, an overall rate (in mol CO_2 produced/cm^2/s) must be estimated from the data. This is accomplished using the formula

$$r\left(\frac{\text{mol CO}_2}{\text{cm}^2\ \text{s}}\right) = \frac{Q\left(\frac{1}{s}\right)\Delta p_{CO_2}(\text{Torr})}{R\left(\frac{\text{Torr 1}}{\text{mol K}}\right)T_b(K)S_c(\text{cm}^2)}, \quad (4)$$

where Q is the actual volumetric gas flow rate through the chamber, Δp_{CO_2} is the measured CO_2 effluent pressure above background, R is the gas constant, T_b is the bulk gas temperature (=298 K), and S_c (= 1.79 cm^2 based on both sides exposed). The actual flow rate is likely to be lower than its upper bound value of 20 liter/s in the steady-state runs. The assumed value for Q is discussed below.

The measured rate multiplicity features are conveniently displayed as the loci of the ignition and extinction points in four different planes. Figures 1 and 2 show the four projections (points are data). Figure 1a is the bifurcation map in the T–p_{CO} plane for $p_{O_2} = 4 \times 10^{-7}$ Torr. The map has the shape of an inverted cusp. For sufficiently high T rate multiplicity was not obtained for any p_{CO}. The rates (r) at the singular points are plotted in the T–r plane in Fig. 1b. Fig. 2a is the bifurcation map in the oxygen pressure (p_{O_2})–CO pressure (p_{CO}) plane for a fixed catalyst temperature (T) of 465.3 K. The map is an upright cusp. For sufficiently low p_{O_2} rate multiplicity was not obtained for any p_{CO}. The corresponding rates (r) at the singular points are plotted in the p_{O_2}–r plane in Fig. 2b.

Figure 3 shows the results of a typical experiment in which the rate–CO pressure dependence was in the form of a clockwise hysteresis loop.

Description of the Parameter Estimation Scheme

Model simulation of the UHV CO oxidation data is carried out by a parameter estimation scheme involving a simultaneous fit of singular and nonsingular data. The method is a modified version of one developed by Harold and Luss (*17*). Details appear in Appendix B and elsewhere (*18*).

The task is to minimize the objective function Ω given by

$$\Omega = \sum_{j=1}^{N_s} \{\sigma_{11}(p_{CO} - \hat{p}_{CO})_j^2 + \sigma_{22}(r - \hat{r})_j^2\} + \sum_{k=1}^{N_{ns}} \{\sigma_{22}(r - \hat{r})_k^2\} \quad (5)$$

by appropriate adjustments of the unknown kinetic parameters. In Eq. (5) N_s is the number of singular (ignition and extinction) points and N_{ns} the number of nonsingular points. The carats (^) denote experimental measurements. The weight factors σ_{11} and σ_{22} are the reciprocals of the estimated variances associated with the CO pressure ($\hat{p}_{CO}$) and rate ($\hat{r}$) measurements.

The calculated singular point coordinates

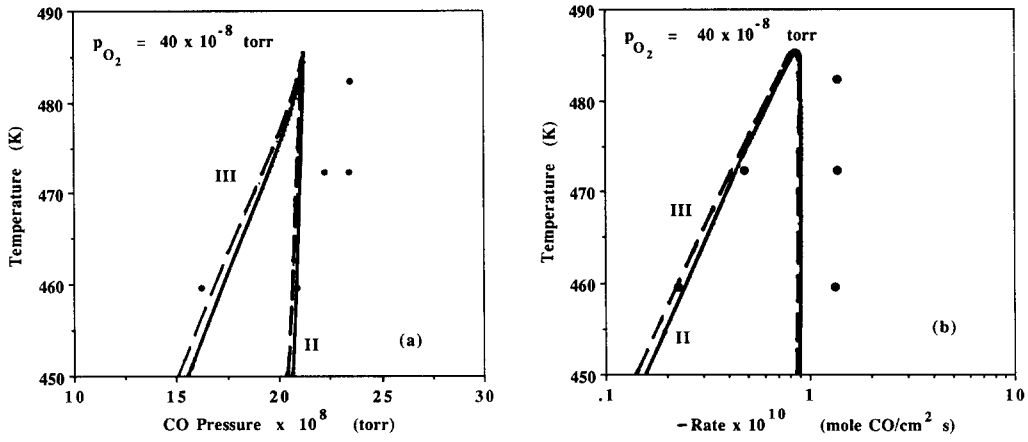

FIG. 1. (a) compares the experimental (solid points) catalyst temperature–CO pressure bifurcation map (fixed oxygen pressure) with model II (solid line) and model III (dashed line) predictions. (b) compares the rates at the same bifurcation points from experiment and model prediction. Data is from Sung (*2*).

(within the first summation of Eq. (5)), p_{CO} and r, are determined by solving simultaneously for θ_{CO} and β_r in

$$F_m(\theta_{CO}, \beta_r, \mathbf{p}_{kn}, \mathbf{p}_{un}) = \frac{dF_m}{d\theta_{CO}} = 0 \quad (m \equiv \text{model II or III}), \quad (6)$$

where $\mathbf{p}_{kn}$ is a vector containing the known (i.e., fixed) kinetic parameters (e.g., sticking coefficients) and operating conditions (e.g., catalyst temperature and oxygen pressure), and $\mathbf{p}_{un}$ is a vector containing the unknown kinetic parameters to be estimated (e.g., some of the E's and k's). A solution (θ_{CO} and β_r), the current estimate for the unknown kinetic parameters, and the particular operating conditions (T and p_{O_2}) are used to compute r and p_{CO}. The calculated rates at the nonsingular points, r (within second summation of Eq. (5)) are determined by solving for θ_{CO} in

$$F_m(\theta_{CO}, \mathbf{p}) = 0 \quad (m \equiv \text{II, III}) \quad (7)$$

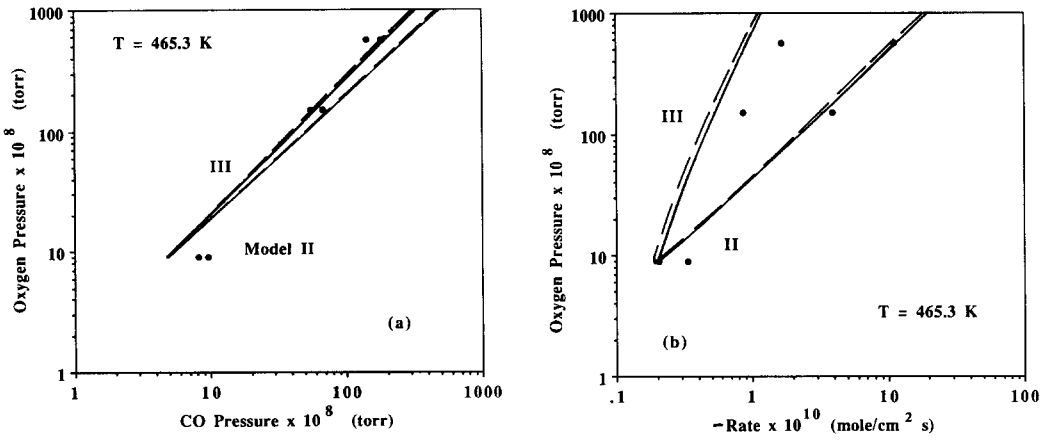

FIG. 2. (a) compares the experimental (solid points) oxygen pressure–CO pressure bifurcation map (fixed temperature) with model II (solid line) and model III (dashed line) predictions. (b) compares the rates at the same bifurcation points from experiment and model prediction. Data is from Sung (*2*).

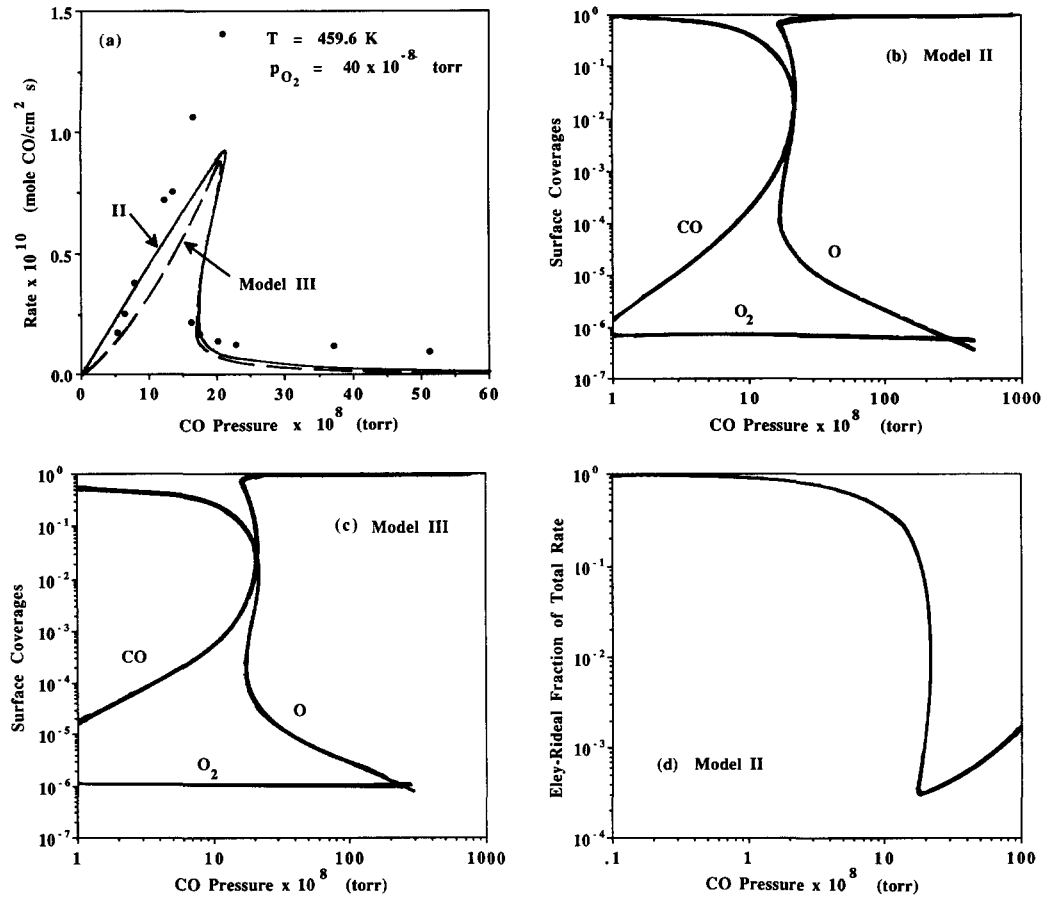

FIG. 3. (a) Comparison of experimental (solid points) rate–CO pressure bifurcation diagram (fixed temperature and oxygen pressure) with model II (solid line) and model III (dashed line) predictions. Data is from Sung (*2*). (b) and (c) respectively show the dependence of the model II and III predicted adsorbate surface coverages as a function of CO pressure. (d) shows the model II predicted contribution by ER steps (7) and (8) to the total rate as a function of the CO pressure.

for a given $\mathbf{p}_{kn}$ and $\mathbf{p}_{un}$. The rate is computed using the solution θ_{CO}, the current estimates for the unknown parameters, and the operating conditions (T, p_{O_2}, and p_{CO}) for the particular point.

A multiresponse, nonlinear optimization scheme is best suited for finding the $\mathbf{p}_{un}$ which minimizes Ω. A modified Levenberg–Marquardt algorithm of Froment and Hosten (*19*) was used. It is described in more detail in Appendix B. The key to a rapid convergence to the minimum of Ω is a reasonable initial guess for $\mathbf{p}_{un}$. Reasonable initial guesses for the four variable parameters $k_{-1}(T_r)$, E_{-1}, k_3 (T_r), and E_3 are available based on literature data. Since only a fraction of the parameters are permitted to vary in the scheme, this minimum is by no means a global one. Thus, although the data fit is not a best fit, the algorithm is essential since any ad hoc method would be an impossible task.

Table 1 lists the experimental measurements of Sung (*2*) which comprised the $\hat{p}_{CO}$ and $\hat{r}$ values in Eq. (17). Six rate–CO pressure multivalued bifurcation diagrams provided a total of six ignition and six extinction points (N_s = 12). The multiplicity was ob-

TABLE 1

Experimental Data of Sung (2) Used in Parameter Estimation Scheme

		Singular data	
T (K)	$p_{O_2} \times 10^8$ (Torr)	$p_{CO} \times 10^8$ (Torr)	$r \times 10^{10}$ (mol CO_2/cm^2 s)
465.3	9	9.51	0.33
		8.19	0.21
465.3	150	67.0	3.91
		54.8	0.86
465.3	560	182.3	11.2
		142.0	1.67
459.6	40	20.89	1.41
		16.22	0.23
472.3	40	23.42	1.37
		22.28	0.48
482.3	40	23.50	1.37
		23.50	1.37
		Nonsingular data	
T (K)	$p_{O_2} \times 10^8$ (Torr)	$p_{CO} \times 10^8$ (Torr)	$r \times 10^{10}$ (mol CO_2/cm^2 s)
459.6	40	31.6	0.186
		100	0.098
465.3	9	10	0.300
		31.6	0.096
465.3	150	100	0.788
		316	0.134
465.3	560	316	1.340
472.3	40	31.6	0.500
		100	0.170
482.3	40	31.6	1.708
		100	0.556
519.4	40	31.6	3.94
		100	1.90
623.4	40	100	5.46
		316	2.40

served for catalyst temperatures between 459.6 and 482.3 K, and for oxygen pressures between 9×10^{-8} and 5.6×10^{-6} Torr (1 Torr = 133.3 N m^{-2}). Either one or two nonsingular points were selected from eight different rate–p_{CO} bifurcation diagrams (single-valued and multivalued) obtained for temperatures between 459.6 and 623.4 K, and oxygen pressures between 9×10^{-8} and 5.6×10^{-6} Torr. These points were all taken from the low-rate branch.

Our estimates for the experimental variance of the CO pressure and rate measurements are $1/(\sigma_{11})^2 = 2 \times 10^{-15}$ Torr^2 and $1/(\sigma_{22})^2 = 10^{-22}$ (mol/cm^2 s)^2, respectively. These estimates give more weight to the CO pressure measurement. The uncertainty in the pumping rate makes the rate estimates more uncertain (Eq. (4)).

The qualitative isothermal rate multiplicity features observed by Sung (2) can be predicted by the models developed in the first part of this study (1). It should be pointed out that Eisworth and Ertl (20) and Eisworth *et al.* (21) reported evidence for a (1×2) to (1×1) reconstruction of Pt(110) during CO oxidation, which led to sustained oscillatory behavior. No such oscillations were reported by Sung (2). Thus, it is not clear that reconstruction played a significant

role in the experiments. For this reason, our simulations do not account for it. Nevertheless, the models could be modified to include the key effect of reconstruction in altering the oxygen sticking coefficient; e.g., a discontinuous function could be used,

$$S_O = S_{O,1}H(\theta_{CO}) - (S_{O,1} - S_{O,2})H(\theta_{CO} - \theta^*_{CO}),$$

where H is the Heaviside function, $S_{o,i}$ is the initial sticking coefficient on structure i, and θ^*_{CO} is the critical CO coverage at which the reconstruction occurs. Such a modification is expected to magnify the differences between the two kinetic regimes and hence make rate multiplicity even more likely.

Models II and III consist of a rather large number of parameters. Those common to each include k_1, $k_{-1}(T_r)$, E_{-1}, k_2, $k_3(T_r)$, E_3, k_4, $k_5(T_r)$, E_5, $k_6(T_r)$, and E_6. Model II contains in addition the Eley–Rideal rate constants k_7 and k_8; model III contains in addition the reciprocal of the maximum fraction of surface covered by oxygen, f. Our approach is to assign four of the parameters to the unknown parameter vector, $\mathbf{p}_{un}$; these are $k_{-1}(T_r)$, E_{-1}, $k_3(T_r)$, and E_3. Clearly, a better data fit is possible by increasing this number (i.e., dimension of $\mathbf{p}_{un}$). The remaining parameters are assigned fixed values based on physical constraints and arguments, or information provided by Sung (2) or other studies (e.g., (7)). The algorithm works best if multiplicity is predicted for all of the conditions for which it was observed experimentally.

The choices for the fixed parameters are now discussed. The adsorption rate constants k_1, k_2, and k_4 are given by the expressions

$$k_1 = \sqrt{\frac{1}{2\pi M_{CO} R T_b}}\, S_{CO}$$

$$k_2 = k_4 = \sqrt{\frac{1}{2\pi M_{O_2} R T_b}}\, S_O, \quad (8)$$

where S_{CO} and S_O are the CO and oxygen sticking coefficients, and T_b is the bulk gas temperature (298.15 K). The oxygen sticking coefficient on Pt(110) is between 0.1 and 1 (7). We assume $S_O = 0.10$ for both atomic and molecular oxygen adsorption; i.e., $k_2 = k_4$. A sticking coefficient for CO of 0.70 was determined by Sung using TPD. We found that the experimental rates calculated based on a pumping rate (Q) of 20 liter/s were too high to be predicted by any of the models when using a CO sticking coefficient of 0.70. In fact, CO sticking probabilities exceeding unity were required to predict the rates based on $Q = 20$ liter/s. Given that the CO sticking coefficient was measured independently, this suggested to us that the actual flowrate was less than 20 liter/s. A decreasing dependence of the pumping rate on the total pressure would help to explain why the Δp_{CO_2}–p_{CO} data revealed a (−0.5)-order dependence in the CO inhibition regime. An assumed value of $Q = 10$ liter/s gave rates which were more reasonable in light of the $S_{CO} = 0.70$ constraint. Clearly, this uncertainty in the value of Q (and hence the rates) reduces the confidence in the estimates for the kinetic parameters. However, we again emphasize that our goals are to predict the correct qualitative multiplicity features, to predict the location of the bifurcation points reasonably, and to satisfy kinetic trends.

The rate constants associated with molecular oxygen dissociation, $k_5(T)$, and reaction of molecular oxygen with adsorbed CO, $k_6(T)$ are assigned values as follows. The molecular oxygen dissociation step (5) is expected to be quite rapid compared to the other reactions. We let $\delta = k_5(T)/k_3(T) = 100$ to reflect this. The termolecular reaction step (6) is likely to be slower than the bimolecular reaction step (3). We let $\eta = k_6(T)/k_3(T) = 0.1$ to reflect this. These assignments ensure a low coverage of molecular oxygen relative to the CO coverage for the CO-covered surface, and relative to the atomic oxygen coverage for the oxygen-covered surface.

For model II the Eley–Rideal rate constants k_7 and k_8 are assumed temperature independent and equal to the CO adsorption

TABLE 2

Set of Parameters Estimated for Model II Simulation of Sung (2) Data

$k_1 = 4.48 \times 10^{-4}$ mol/cm^2 s Torr ($S_{CO} = 0.70$)
$k_{-1}(T_r) = 1.00 \times 10^{-11}$ mol/cm^2 s[a]
$E_{-1} = 30.69$ kcal/mol[a]
$k_2 = 6.0 \times 10^{-5}$ mol/cm^2 s Torr ($S_O = 0.10$; atomic oxygen)
$k_3(T_r) = 4.47 \times 10^{-7}$ mol/cm^2 s[a]
$E_3 = 21.85$ kcal/mol[a]
$k_4 = 6.0 \times 10^{-5}$ mol/cm^2 s Torr ($S_O = 0.10$; molecular oxygen)
$\delta = k_5(T)/k_3(T) = 100$
$\eta = k_6(T)/k_3(T) = 0.10$
$\xi = k_7/k_1 = 1.0$
$\kappa = k_8/k_1 = 1.0$

[a] Parameters that were allowed to vary in the estimation scheme; the others were fixed at indicated values.

constant ($\xi = k_7/k_1 = 1$; $\kappa = k_8/k_1 = 1$). The former assumption reflects the fact that the Eley–Rideal reaction between gas phase or weakly adsorbed mobile CO with adsorbed oxygen is essentially a nonactivated process. The latter assumption implies that the probability for the Eley–Rideal type reaction is equal to the CO sticking probability.

For model III we assume a maximum coverage by oxygen species to be 0.5 (i.e., $f = 2$). This agrees with measurements of McCabe and Schmidt (*22*) and Conrad *et al.* (*23*).

Results and Discussion

Figures 1a, b and 2a, b compare the model II and III predictions of the four singular point projections with the experimental measurements. The points are the data. Figure 3a shows the model II and III simulations of a typical rate–CO pressure bifurcation diagram. Recall that one or two nonsingular points from eight bifurcation diagrams were used as experimental observations (Table 1). Tables 2 and 3 respectively provide the fixed and estimated kinetic parameters.

The catalyst temperature (T)–CO pressure (p_{CO}; Fig. 1a) and temperature–rate (Fig. 1b) projections (fixed oxygen pressure) are simulated reasonably well by each model. The models predict the inverted cusp T–p_{CO} map and the approximate location of the cusp. The slopes of the ignition and extinction loci in the T–p_{CO} map are slightly larger than the experimental slopes. As a result, the CO pressure range for which multiplicity is predicted for $T \geq 472.3$ K is somewhat less than the experimental range. In addition, the extinction rates are under-predicted (Fig. 1b).

The oxygen pressure (p_{O_2})–CO pressure (p_{CO}) (Fig. 2a), and p_{O_2}–rate (Fig. 2b) projections (fixed T) are also predicted reasonably well. The models predict the rather narrow upright cusp shape of the p_{O_2}–p_{CO} map. For the p_{O_2}–p_{CO} projection the slopes of the ignition and extinction loci are below the experimental values (Fig. 2a). The ignition rates are not surprisingly the most poorly predicted response (Fig. 2b).

Figures 3a–3d provide more details about the differences in the model II and III simulations than the predicted projections (Figs. 1 and 2), which are virtually indistinguishable. Each model correctly predicts the clockwise dependence of the rate (r) on p_{CO} (Fig. 3a). Along the upper rate branch the experimental order varies between 2 (low

TABLE 3

Set of Parameters Estimated for Model III Simulation of Sung (2) Data

$k_1 = 4.48 \times 10^{-4}$ mol/cm^2 s Torr ($S_{CO} = 0.70$)
$k_{-1}(T_r) = 8.65 \times 10^{-12}$ mol/cm^2 s[a]
$E_{-1} = 32.81$ kcal/mol[a]
$k_2 = 6.0 \times 10^{-5}$ mol/cm^2 s Torr ($S_O = 0.10$; atomic oxygen)
$k_3(T_r) = 2.98 \times 10^{-7}$ mol/cm^2 s[a]
$E_3 = 22.49$ kcal/mol[a]
$k_4 = 6.0 \times 10^{-5}$ mol/cm^2 s Torr ($S_O = 0.10$; molecular oxygen)
$\delta = k_5(T)/k_3(T) = 100$
$\eta = k_6(T)/k_3(T) = 0.10$
$f = 2.0$

[a] Parameters that were allowed to vary in the estimation scheme; the others were fixed at indicated values.

p_{CO}) and near unity near the extinction point. Model II predicts a first-order rate dependence on p_{CO} for most of the branch. Model III predicts a more nonlinear dependence along the upper branch, which is in closer agreement with the data. It was demonstrated in the first part of this study that both models II and III are capable of predicting a reaction order between 1 and a very high value for $p_{CO} \to 0$. The fact that model III better predicts a first-order rather than second-order rate dependence for this particular set of parameters suggests that the assumed Eley–Rideal reaction probabilities may be too large.

Along the low rate branch (high p_{CO}/p_{O_2}) in Sung's data the experimental order is about -0.5. Both models predict a (-1)-order for high p_{CO}, which agrees with most other CO oxidation experiments (*6*). Again, the unusually high experimental order (-0.5) may be attributed to other experimental factors such as a variable pumping rate.

The predicted surface coverages provide more insight into the data simulation. Figures 3b and 3c show the model II and III predicted dependence of the CO, atomic and molecular oxygen coverages on p_{CO} for the conditions corresponding to Fig. 3a. Models II and III both predict a CO coverage (θ_{CO}) increase from near zero to unity as p_{CO} increases. Each θ_{CO} curve is multivalued and in the form of a counterclockwise hysteresis loop. Note that model III predicts a higher CO coverage for low p_{CO} because of the incomplete coverage by oxygen species. However, the rates are nearly equal despite this difference since for model II CO reacts by the Eley–Rideal mechanism without a need for a site. The atomic oxygen coverage is in the form of a clockwise hysteresis loop. Each model predicts a low molecular oxygen coverage over the entire p_{CO} range. For p_{CO} below approximately 100×10^{-8} Torr each model predicts that $\theta_{O_2} \approx \Gamma/\delta$. For higher p_{CO}, θ_{O_2} decreases. However, the atomic oxygen coverage decreases more rapidly because of the two-site requirement for dissociative oxygen adsorption (i.e., second-order dependence on vacant site coverage). For sufficiently high p_{CO}, θ_{O_2} exceeds θ_O (as in Fig. 3b). This demonstrates that single-site oxygen adsorption becomes competitive with atomic oxygen adsorption when CO occupies most of the available sites. Moreover, the molecular oxygen coverage need not be large in order for both models to predict the observed kinetic behavior.

It is quite revealing to check the model II predicted fractional contribution to the total rate by the Eley–Rideal reaction steps (7) and (8). Figure 3d shows the dependence of the Eley–Rideal fraction on p_{CO} corresponding to the experimental conditions of Fig. 3a. The fractional dependence exhibits a local minimum. For $p_{CO} \ll p_{O_2}$ ($= 40 \times 10^{-8}$ Torr) the ER reaction dominates because of the high oxygen surface coverage. In this regime the rate is first-order with respect to CO. Over a wide range of intermediate p_{CO} the Langmuir reaction dominates. For high p_{CO} the ER contribution increases. In this regime the ER reaction is unlimited in a sense since CO does not have to adsorb in order to react. This trend is not significant during UHV operation; Fig. 3d shows that the ER contribution is less than 0.1% of the total rate for $p_{CO}/p_{O_2} = 2.5$. However, this trend has important implications for higher pressure operation, as shown later.

The estimates for the four parameters $k_{-1}(T_r)$, E_{-1}, $k_3(T_r)$, and E_3 provided in Tables 2 and 3 are in good agreement with literature values. The CO desorption activation energy (E_{-1}) is estimated to be 30.7 and 32.8 kcal/mol by models II and III, respectively. As we showed in the first part, in the CO inhibition regime the activation energy is essentially equal to E_{-1}. The estimated values are quite close to the 30.5 kcal/mol value estimated by Sung (*2*), and to other reported values (*7, 3*). The CO desorption frequency factors are less than the 2×10^4 value based on a Polyani–Wagner desorp-

tion process. Deviations from the Polyani–Wagner value are not uncommon (*7*, *6*). Finally, the Langmuir reaction step (3) parameters are well within other UHV determined values (*6*).

The quite similar performance of models II and III in simulating Sung's UHV data precludes a definitive discrimination. Each simulates the singular point data equally well. Model III predicts the experimentally observed nonlinear order along the high rate branch. However, model II should predict equally well the order for a lower value of the Eley–Rideal reaction constants. The uncertain contribution of the ER reaction based on insufficient direct UHV evidence may suggest that model III is more firmly rooted on physical grounds.

It should be pointed out that an attempt was also made to simulate the data using the $CO–O_2$ site exclusion model IV. This model could not simulate the data as well as models II and III. While this is by no means sufficient to rule out model IV, it is not an unexpected result since most UHV evidence indicates that CO occupies all the available sites on a Pt surface.

INTERMEDIATE PRESSURE CO OXIDATION

In this section models II and III are used to simulate CO oxidation at intermediate pressure; i.e., CO and oxygen pressures in the 10^{-3}–10 Torr range without a diluent present (i.e., subatmospheric pressure operation). Our aim is to link intermediate pressure with UHV kinetic behavior. The kinetic parameter values estimated from the simulation of Sung's UHV data are used to simulate the higher pressure CO oxidation experiments.

In the first part of this section model II and III predictions are compared with intermediate pressure experiments in the CO inhibition regime in order to further discriminate between models II and III. In the second part we check the impact of increased pressure on the multiplicity features.

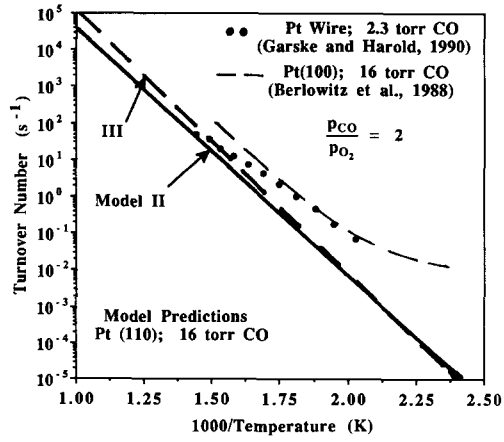

FIG. 4. Comparison of the turnover number–reciprocal temperature data for Pt(100) (Berlowitz *et al.* (*3*)) and Pt wire (Garske and Harold (*4*, *5*)) with the model II and III predictions using the kinetic parameters estimated from the UHV data simulation (Tables 2 and 3).

CO Oxidation on Pt(100) (Berlowitz et al. (3) and Pt Wire (Garske and Harold (4, 5))

Two sets of intermediate pressure CO oxidation data are shown in Fig. 4a as the turnover number (TON) dependence on the reciprocal of the catalyst temperature ($1/T$) for a stoichiometric mixture; i.e., $p_{CO}/p_{O_2} = 2$. In the first set, CO oxidation was carried out on a single Pt(100) crystal by Berlowitz *et al.* (*3*), with $p_{CO} = 16$ Torr and $p_{O_2} = 8$ Torr. In the second set reaction was carried out on a polycrystalline Pt wire in our laboratory, with $p_{CO} = 2.3$ Torr and $p_{O_2} = 1.15$ Torr. Details of the latter study are reported elsewhere (*5*).

The Pt(100) data of Berlowitz *et al.* (*3*) reveals that for $T > 500$ K the rate is (-1)-order in CO with an apparent activation energy of about 33 kcal/mol. As the temperature is decreased from 500 K to 420 K a change in the CO reaction order and activation energy is noted; the order increases from (-1) to zero and the activation energy decreases to about 13 kcal/mol. The kinetic behavior at high temperatures agrees qualitatively quite well with a number of studies

of CO oxidation in the CO inhibition regime (e.g., (*24, 7*)). The behavior at lower temperature matches very well the data of Cant *et al.* (*9*) for CO oxidation on a 5% Pt/SiO_2 catalyst. Similar near zero-order and low activation energies have been reported by others for various Pt catalysts (e.g., (*25, 26*)).

The Pt wire data for Garske and Harold (*4, 5*) exhibits an apparent activation energy of about 24 kcal/mol. The order with respect to CO (oxygen) is 1 (−1). No evidence for a transition to different behavior at lower temperatures was observed.

It is of interest to check if models II and III predict these trends obtained from two different experiments at intermediate pressure. Figure 4 shows the model II and III predictions. No parameter values were changed from those estimated in the Sung Pt(110) data simulation (Tables 2 and 3). Both models II and III predict a near linear dependence of ln(TON) on $1/T$ for the entire temperature range. The apparent activation energy is close to 30.7 (32.8) kcal/mol for model II (III), the estimated CO desorption activation energy (E_{-1}). This is in good agreement with the Garske and Harold data and the linear portion of the Berlowitz *et al.* data. However, the lower temperature features are not as well predicted. This discrepancy is considered shortly.

A key point is worth noting regarding model II. As the temperature is increased from 400 to 1000 K the CO coverage decreases monotonically from near unity but the reaction order with respect to CO remains (−1). Moreover, the contribution to the overall rate by the Eley–Rideal steps (7) and (8) decreases monotonically. Despite this shift in contribution, the predicted rate remains first order in oxygen and (−1) order in CO over the entire range of temperature. These results show that the ER pathway does not alter the kinetic features in the CO inhibition regime. For this reason, and the rather low rates, it may be difficult to experimentally distinguish between the Langmuir and ER steps in steady-state experiments at these pressures.

Similarly, the oxygen exclusion feature of model III does not alter the kinetics in the CO inhibition regime. In the first part of this study a limiting rate expression was derived for the case in which molecular oxygen adsorption dominates dissociative oxygen adsorption, and the molecular oxygen coverage is much less than the CO coverage, which is assumed equal to its equilibrium value. These conditions give the rate expression (*1*):

$$\text{Rate} = \frac{2k_6(T)\Gamma/\eta[\beta^2 + (f-1)\Gamma(1+\beta)/\eta]^2}{(1+\beta)[\beta^2 + f\Gamma(1+\beta)/\eta]^3}. \tag{9}$$

Using the values for $k_{-1}(T_r)$, E_{-1}, k_2, $k_6(T)$, and f (Table 3), it is confirmed that Eq. (9) describes the observed kinetic behavior well; i.e., an apparent activation energy equal to E_{-1} and a rate that is 1 (−1) order in O_2(CO). Moreover, the implicit assumptions in deriving (9) are satisfied.

An obvious question at this point is what modification of models II and III is necessary to predict the low-temperature behavior evident in the Berlowitz *et al.* (*3*) data. One possibility is the repulsive interaction between adsorbed CO molecules. It is known that the CO heat of adsorption ($-\Delta H_{a,CO} = E_{-1} - E_1$) is a decreasing function of θ_{CO}. To a first approximation, $(-\Delta H_{a,CO}) = (-\Delta H^0_{a,CO}) - h\theta_{CO}$, where h can be as high as 7 kcal/mol (*6*). This is clearly not a large enough difference to account for a nearly 20 kcal/mol energy decrease in the Pt(100) data. Moreover, the binding energy dependence does not adequately explain the shift in CO reaction order.

A more likely possibility is an Eley–Rideal type pathway for CO_2 formation from a CO-covered surface. Cant *et al.* (*9*) suggested that reaction may occur between adsorbed CO and molecular oxygen adsorbed on top of the CO layer. Such a step is described by

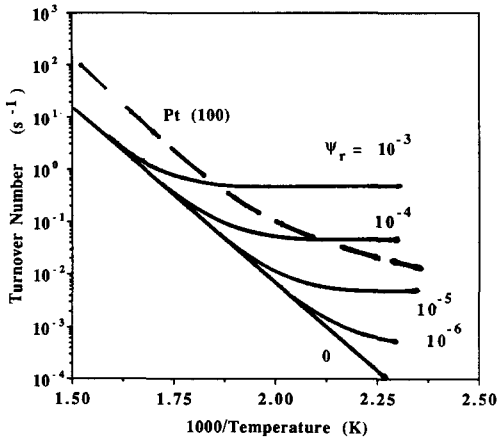

FIG. 5. The impact of the rate constant for the ER step (10) ($\Psi_r = k_{10}p_{O_2}/k_3(T_r)$) on the model II predicted rate dependence on temperature (solid line). The data of Berlowitz *et al.* (*3*) is shown for comparison.

$$(10): \quad O_2 + CO\text{–}X \rightarrow CO_2 + O\text{–}X \quad (10)$$

The CO_2 formation rate from this step is equal to $k_{10}p_{O_2}\theta_{CO}$. Step (10) is easily incorporated into either model II or III.

The impact of step (10) on the model II rate predictions is demonstrated in Fig. 5 which shows the dependence of the turnover number on reciprocal temperature for several values of $\Psi_r = k_{10}p_{O_2}/k_3(T_r)$. The Berlowitz *et al.* (*3*) data is shown for comparison. The $\Psi_r = 0$ case corresponds to the model II simulation in Fig. 4. As Ψ_r is increased slightly from zero the essentially negatively sloped straight line bends up at lower temperatures. The $\Psi_r = 10^{-3}$, 10^{-4}, and 10^{-5} cases show that for sufficiently low temperature the turnover number is independent of temperature. Indeed, in this regime of reduced apparent activation energy our calculations reveal that the rate is first order in oxygen and zero order in CO. It is interesting to note in Fig. 5 that the $\Psi_r = 10^{-6}$ case demonstrates a shift in the apparent activation energy from 30.7 kcal/mol at high temperature to approximately 8 kcal/mol at 445 K. Except for the difference in absolute rate, this shift is quite similar to the experimental shift in the Berlowitz *et al.* data. A value of $\Psi_r = 10^{-6}$ implies that the ratio of the reaction step (10) probability is less than 10^{-7}% of the oxygen sticking probability (i.e., $2\Psi_r/\gamma_r = k_{10}/k_2 = 9.3 \times 10^{-10}$). However, our calculations reveal that the step (10) contribution exceeds 15% of the total rate for $T < 470$ K. This suggests that although the Eley–Rideal reaction step (10) probability is quite small, it can still have a major impact on the rate for a CO-covered surface. Unfortunately, experimental verification could be quite difficult.

Effect of Increasing Pressure on Rate Multiplicity Features

Besides the questions about the basic kinetic features in linking UHV and higher pressure CO oxidation, another key question is whether multiplicity observed under UHV conditions is observed at intermediate pressure, or vice versa.

Figure 6 shows the model II predicted evolution of the temperature–CO pressure bifurcation map as the oxygen pressure is

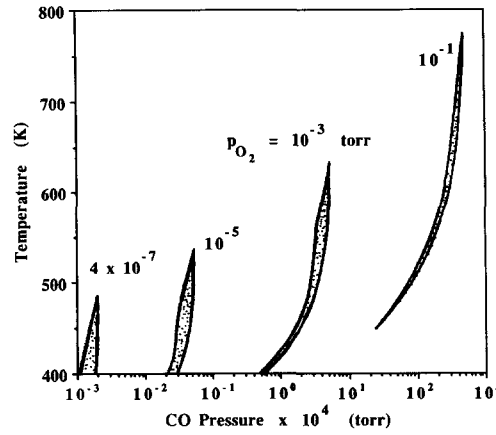

FIG. 6. Model II predicted impact of the oxygen pressure on the temperature–CO pressure bifurcation map. The $p_{O_2} = 4 \times 10^{-7}$ Torr map is from the simulation of Sung's (*2*) data (Fig. 1a). Parameter values are listed in Table 2.

increased from its level in the Sung data simulations (4×10^{-7} Torr) to 0.1 Torr. All the kinetic parameters remain fixed at their values in Table 2. Figure 6 reveals that rate multiplicity persists as the pressure is increased. However, its shape changes from an inverted cusp at UHV conditions to a closed region formed by high and low temperature cusps at higher pressures. At the higher oxygen pressures multiplicity is predicted to occur at higher temperatures but over a narrower range of CO pressure.

The disappearance of multiplicity at a sufficiently high temperature is a result of the increased rate of CO desorption and a shift of the CO inhibition state to very high CO pressures relative to the oxygen pressure. The existence of a low-temperature cusp is a result of both the adsorbed molecular oxygen steps (4)–(6) and the Eley–Rideal steps (7) and (8). It was shown in the first part that the limiting case models, in which (i) oxygen adsorbs only molecularly, or (ii) reaction occurs only by the ER mechanism, cannot predict rate multiplicity. The latter effect appears to be the principle cause for the appearance of the low-temperature cusp. The ER reactions, being nonactivated, become more competitive with the activated Langmuir reaction steps at low temperature if the reactant pressures are sufficiently high. Multiplicity vanishes at sufficiently low temperature due to this shift. This feature is not observed at UHV because the reactant pressures are not high enough to make the ER reaction path competitive with the Langmuir reaction path over a wide range of temperature and p_{CO}/p_{O_2}.

ATMOSPHERIC PRESSURE CO OXIDATION: IMPACT OF MASS TRANSPORT RESISTANCE

In experimental studies of CO oxidation at intermediate to high pressures it is difficult to avoid mass transport limitations. As a result, it can be quite difficult to differentiate between true intrinsic rate multiplicity and multiplicity caused by a coupling of single-valued intrinsic kinetics and mass transport. The aim of this section is to demonstrate how mass transport limitations affect the multiplicity features (e.g., bifurcation map shape) for a Pt-catalyzed CO oxidation reaction system that exhibits intrinsic rate multiplicity. As pointed out in the first part, the shape of the temperature–CO pressure bifurcation map is different than the inverted cusp observed in transport-limitation-free experiments (e.g., UHV operation). First we describe two sets of atmospheric pressure experimental data in which mass transport limitations are important. Then kinetic model II is modified to include external mass transport resistance.

Atmospheric Pressure CO Oxidation on a Pt/SiO_2 Wafer (Kaul et al. (6))

Kaul *et al.* (*6*) reported rate multiplicity for the atmospheric pressure oxidation of CO on a Pt/SiO_2 wafer in a flow-through cell with external recycle. Two different "catalyst gas" temperature–CO inlet concentration bifurcation maps were observed. Each map has a monotonically increasing ignition branch. The extinction branch features depended on the oxygen concentration. For high oxygen concentration the extinction branch has a local maximum; the map resembles type (d) in Fig. 1 of the first part of this study (*1*). For low oxygen concentrations the extinction branch is monotonic but exhibits a large slope near the stoichiometric ratio $p_{CO}/p_{O_2} = 2$; this resembles map type (c) in Fig. 1 of the first part. The extinction maximum can be attributed to a thermokinetic interaction (*17*).

It is of interest to determine if the map features observed by Kaul *et al.* (*6*) can be predicted by model II. The sharp transition in the extinction branch is a new feature that is not seen in our earlier simulations. The design and operation of the single wafer experiment suggests that external mass transport resistance is significant under some conditions. The key evidence is that at high temperature the extinction occurs near the overall stoichiometric point. This indicates that the bulk phase supply rates are crucial

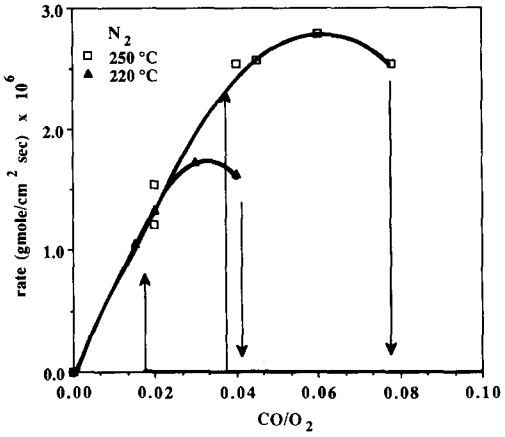

FIG. 7. Dependence of the Pt wire-catalyzed CO oxidation rate on CO pressure at two average wire temperatures. Nitrogen is the diluent.

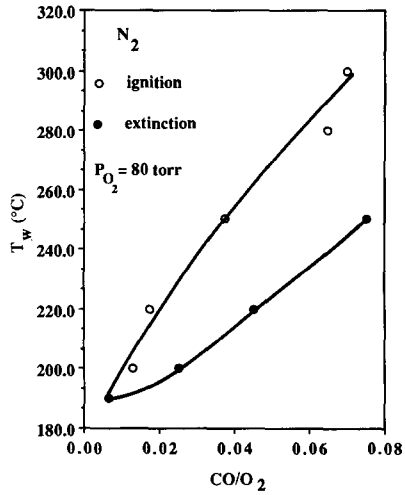

FIG. 8. Average wire temperature–CO pressure bifurcation map using nitrogen as diluent.

in determining the rate. To address these questions, external mass transport resistance must be incorporated into the model.

Atmospheric Pressure CO Oxidation on a Pt Wire (Garske and Harold (4, 5))

Steady-state rate multiplicity was observed for CO oxidation at atmospheric pressure on an electrically heated Pt wire carried out in our laboratory. The average wire temperature (T_w) was controlled by a constant temperature anemometer. A mixture of CO, oxygen, and nitrogen or helium flowed over the 3-cm-long, 0.005-cm-diameter wire with a linear velocity of approximately 2 cm/s. A detailed report of the experimental findings was presented recently and will appear elsewhere (*4, 5*).

Figure 7 shows two rate versus CO/O_2 bifurcation diagrams obtained for $T_w = 220$ and 250°C using nitrogen as the diluent. The clockwise hysteresis loop expands and moves to higher CO/O_2 as T_w is increased. In this set of experiments the rates along low-branch states to the right of the ignition points were not measured accurately and are represented by a horizontal line at zero rate. Our interest focused on locating the CO/O_2 value resulting in ignition. The low branch rates were measured in other experiments (e.g., see Fig. 4 and (*5*)). Figure 8 shows the T_w–CO/O_2 bifurcation map with nitrogen as the diluent. It is a cusp oriented upward.

Figures 9 and 10 show similar results obtained with helium as the diluent. Figure 9 presents two typical rate–CO/O_2 diagrams obtained for $T_w = 250$ and 280°C. They are clockwise hysteresis loops. The T_w–CO/O_2 bifurcation map shown in Fig. 10 is an upright cusp.

A comparison of the nitrogen (Figs. 7 and 8) and helium (Figs. 9 and 10) data reveals identical qualitative features. However, a higher wire temperature is needed to encounter multiplicity for some CO concentrations when using helium as the diluent. Moreover, the cusp-shaped region appears to be somewhat narrower than the region obtained using nitrogen.

Substitution of helium for nitrogen as the diluent serves to enhance the rate of external heat and mass transport. The enhanced mass transport reduces the extent of external transport limitations. Thus, if rate multiplicity vanishes in switching from nitrogen to helium, this is evidence that the multiplicity obtained with nitrogen results from the interaction of external mass transport and

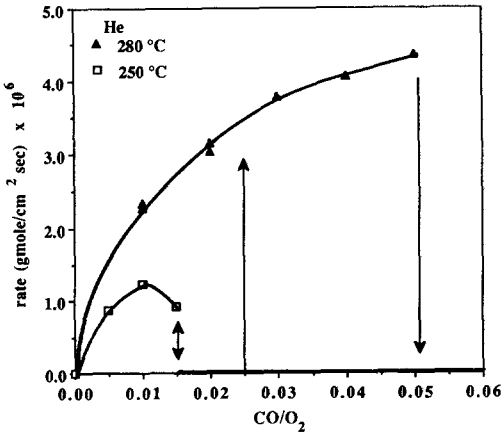

FIG. 9. Dependence of the Pt wire-catalyzed CO oxidation rate on CO pressure at two average wire temperatures. Helium is the diluent.

an intrinsic rate which is single valued and which simply exhibits a maximum at an intermediate CO concentration. However, the fact that rate multiplicity persists in switching to helium is evidence that the multiplicity is due at least partially to the kinetics alone. This conclusion is supported by experiments carried out at subatmospheric pressure that reveal the persistence of multiplicity (*4, 5*). It is of interest to determine if the trends exhibited by the data (Figs. 8, 10) are consistent with the model II predictions with mass transport incorporated.

One point that is not in the central theme of our study but is worth noting is the apparent impact of the diluent on the intrinsic kinetic behavior. A comparison of the bifurcation diagrams obtained using nitrogen (Fig. 7) and helium (Fig. 9) reveals that for the same average wire temperature the low rate, kinetic-controlled state can be sustained at lower CO/O_2 values when using helium as the diluent compared to nitrogen. If the diluent type does not affect the kinetics there should be little if any change in the rate along the low-rate state. The diluent type should only alter the high-rate mass transport limited state. Our data are in agreement with the findings of Chakrabarty *et al.* (*27*) who showed that the CO oxidation rate in the CO inhibition regime increases with increasing diluent molecular weight. This collision-induced desorption process was more recently discussed by Ceyer (*28*).

Incorporation of Mass Transport Resistance into Model

External mass transport processes are now incorporated into kinetic model II. The supply rates of CO and oxygen to the catalyst surface are equal to their respective rates of consumption:

$$k_{pCO}(p_{bCO} - p_{CO}) = k_3\theta_{CO}\theta_O + 2k_6\theta_{CO}^2\theta_{O_2} + k_7 p_{CO}\theta_O + k_8 p_{CO}\theta_{O_2} \quad (11)$$

$$2k_{pO_2}(p_{bO_2} - p_{O_2}) = k_3\theta_{CO}\theta_O + 2k_6\theta_{CO}^2\theta_{O_2} + k_7 p_{CO}\theta_O + k_8 p_{CO}\theta_{O_2}, \quad (12)$$

where b denotes bulk and k_{pi} is the mass transport coefficient for species i. The dimensionless surface-to-bulk pressure ratios are defined as

$$\rho_{CO} = \frac{p_{CO}}{p_{bCO}} \quad \rho_{O_2} = \frac{p_{O_2}}{p_{bO_2}}. \quad (13)$$

Upon nondimensionalization of Eqs. (11) and (12), two new parameters that are inversely proportional to the transport coefficients result:

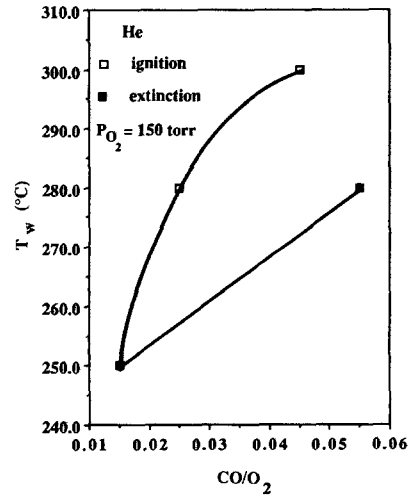

FIG. 10. Average wire temperature–CO pressure bifurcation map using helium as the diluent.

$$\varepsilon_{CO} = \frac{k_1}{k_{pCO}} \quad \varepsilon_{O_2} = \frac{k_2}{k_{pO_2}}. \tag{14}$$

The model parameters β and γ are redefined based on the bulk pressure of CO and of oxygen:

$$\beta_b = \frac{k_1 p_{bCO}}{k_{-1}} \quad \gamma_b = \frac{2k_2 p_{bO_2}}{k_3}. \tag{15}$$

Applying Eqs. (13), (14), and (15) to Eqs. (11) and (12), and solution for ρ_{CO} and ρ_{O_2} gives

$$\rho_{CO} = \frac{\varepsilon_{CO}^{-1} - \frac{\alpha}{\beta_b}(\theta_{CO}\theta_O + 2\eta\theta_{CO}^2\theta_{O_2})}{\varepsilon_{CO}^{-1} + \xi\theta_O + \kappa\theta_{O_2}} \tag{16}$$

$$\rho_{O_2} = 1 - \frac{\varepsilon_{O_2}}{\gamma_b}\left[\theta_{CO}\theta_O + 2\eta\theta_{CO}^2\theta_{O_2} + \frac{\rho_{CO}\beta_b}{\alpha}(\xi\theta_O + \kappa\theta_{O_2})\right]. \tag{17}$$

The governing CO, atomic and molecular oxygen balances are modified to accommodate the external transport resistance using $p_{CO} = \rho_{CO} p_{bCO}$ and $p_{O_2} = \rho_{O_2} p_{bO_2}$:

$$F_1 \equiv \beta_b \theta_{v,CO}\rho_{CO} - \theta_{CO} - \alpha\theta_{CO}\theta_O - 2\eta\alpha\theta_{CO}^2\theta_{O_2} = 0 \tag{18}$$

$$F_2 \equiv \gamma_b \theta_{v,O}^2 \rho_{O_2} - \theta_{CO}\theta_O + 2\delta\theta_{O_2}\theta_{v,O} - \frac{\beta_b}{\alpha}\xi\theta_O\rho_{CO} + \frac{\beta_b}{\alpha}\kappa\theta_{O_2}\rho_{CO} = 0 \tag{19}$$

$$F_3 \equiv \Gamma_b \theta_{v,O}\rho_{O_2} - \eta\theta_{CO}^2\theta_{O_2} - \delta\theta_{O_2}\theta_{v,O} - \frac{\beta_b}{\alpha}\kappa\theta_{O_2}\rho_{CO} = 0, \tag{20}$$

where $\theta_{v,CO}$ and $\theta_{v,O}$ are the vacant sites available for CO and oxygen, and ρ_{CO} and ρ_{O_2} are given by (16) and (17), respectively.

Some simulations are now presented to link the atmospheric pressure data of Kaul *et al.* (*6*) and Garske and Harold (*4*, *5*) to the UHV and intermediate pressure findings. Figure 11 shows the model II predictions of the impact of external mass transport on the temperature–CO pressure map for an oxygen pressure fixed at 8 Torr. The

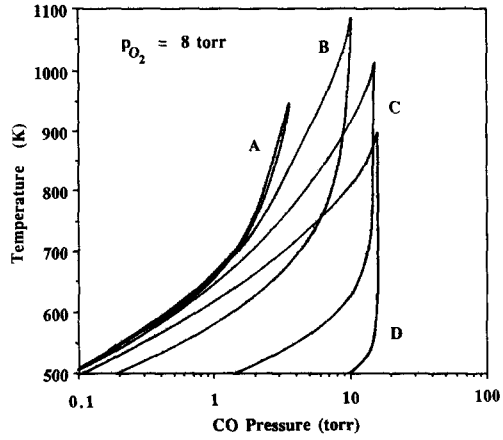

FIG. 11. Impact of the external mass transport resistance on the model II predicted temperature–CO pressure bifurcation maps. Curves A, B, C, and D correspond to $k_{pCO} = k_{pO_2} = 10^{-3}$, 10^{-4}, 10^{-5}, and 10^{-6} mol/cm^2 s Torr, respectively. The oxygen pressure is 8 Torr. All other parameter values are provided in Table 2.

maps are constructed by solving Eqs. (18)–(20) and

$$\begin{vmatrix} \frac{\partial F_1}{\partial\theta_{CO}} & \frac{\partial F_1}{\partial\theta_O} & \frac{\partial F_1}{\partial\theta_{O_2}} \\ \frac{\partial F_2}{\partial\theta_{CO}} & \frac{\partial F_2}{\partial\theta_O} & \frac{\partial F_2}{\partial\theta_{O_2}} \\ \frac{\partial F_3}{\partial\theta_{CO}} & \frac{\partial F_3}{\partial\theta_O} & \frac{\partial F_3}{\partial\theta_{O_2}} \end{vmatrix} = 0. \tag{21}$$

The model II kinetic parameters are assigned the values in Table 2. Map A is a case of negligible transport limitations ($k_{pCO} = k_{pO_2} = 10^{-3}$ mol/cm^2 s Torr). Maps B, C, and D correspond to $k_{pCO} = k_{pO_2} = 10^{-4}$, 10^{-5}, and 10^{-6} mol/cm^2 s Torr, respectively. The transport coefficients k_{pCO} and k_{pO_2} are set equal because the diffusivities for CO and O_2 in diluent are quite close. An estimate for k_{pCO} from our Pt wire experiment can be obtained from the slope of the high rate branch at the origin in a rate–CO pressure diagram (i.e., since $p_{CO} \approx 0$ the rate $\approx k_{pCO} p_{bCO}$). This analysis gives typical values between 10^{-7} and 10^{-6} mol/cm^2 s Torr.

The most dramatic effect of the mass transport limitations is the expansion of the multiplicity region. With negligible limitations the multiplicity region is quite narrow and closes at cusps at high and low temperature. As $k_{pCO} = k_{pO_2}$ are decreased the high-temperature cusp moves to lower temperatures and the low-temperature cusp moves to temperatures below 500 K (not shown).

A revealing feature in Fig. 11 is the shift in the location and the change in slope of the extinction branch as mass transport limitations are increased. For a fixed temperature, the extinction CO pressure moves to higher values and the extinction branch slope becomes much steeper as $k_{pCO} = k_{pO_2}$ are reduced. In fact, the extinction branch is almost vertical for a CO pressure of about 16 Torr (for maps C and D). This corresponds to the stoichiometric ratio, $p_{bCO}/p_{bO_2} = 2$. This feature was observed by Kaul *et al.* (*6*) and Haaland and Williams (*29*) in their atmospheric pressure experiments. Along the extinction branch the rate is limited by mass transport, as ρ_{CO} approaches zero (*18*).

Extinction occurs near the stoichiometric point for severe transport limitations simply because the catalyst cannot sustain a high rate with any CO beyond that required by the overall stoichiometry. As a result, extinction to the low-rate state occurs. This is a trend that is apparently not dependent on the detailed features of the kinetic model. The kinetic model need only exhibit a maximum at an intermediate CO pressure. To illustrate, suppose that the CO oxidation rate is described by

$$\text{Rate}(p_{CO}, p_{O_2}) = \frac{k_r K_{CO} K_{O_2} p_{O_2}}{(1 + K_{CO}p_{CO} + K_{O_2}p_{O_2})^2} = \frac{kp_{CO}p_{O_2}}{(1 + K_{CO}p_{CO} + K_{O_2}p_{O_2})^2}. \quad (22)$$

As pointed out in the first part, Eq. (22) is a rate expression used by many previous investigators. The film balances for CO and oxygen, respectively, satisfy

$$k_{pCO}(p_{bCO} - p_{CO}) = \text{Rate} \quad (23)$$

$$\nu k_{pO_2}(p_{bO_2} - p_{O_2}) = \text{Rate} \quad (24)$$

where $\nu = 2$. Equations (23) and (24) are combined and cast into the dimensionless form

$$F(\theta_{CO}, \mathbf{p}) = (1 - \rho_{CO})[1 + Q_{CO}\rho_{CO} + Q_{O_2}\rho_{O_2}]^2 - D_1\rho_{CO}\rho_{O_2} = 0, \quad (25)$$

where

$$\rho_{O_2} = 1 - \frac{D_2}{D_1}(1 - \rho_{CO}) \quad (26)$$

$$D_1 = \frac{kp_{bO_2}}{k_{pCO}} \quad D_2 = \frac{kp_{bCO}}{\nu k_{pO_2}}$$

$$Q_{CO} = K_{CO}p_{bCO} \quad Q_{O_2} = K_{O_2}p_{bO_2}. \quad (27)$$

The singular set is given by the simultaneous solution of $F(\rho_{CO}, \mathbf{p}) = dF/d\rho_{CO} = 0$. Along the upper rate branch and at the extinction point $\rho_{CO} \approx 0$ for a severely mass transport limited reaction. If we also assume $Q_{O_2} \ll 1$, $F(\rho_{CO}, \mathbf{p}) = 0$ (Eq. (25)) and $dF/d\rho_{CO} = 0$ simplify to

$$F(\rho_{CO}, \mathbf{p}) = (1 + Q_{CO}\rho_{CO})^2 - D_1\rho_{CO}\left(1 - \frac{D_2}{D_1}\right) = 0 \quad (28)$$

$$\frac{dF}{d\rho_{CO}} = -(1 + Q_{CO}\rho_{CO})^2 + 2(1 + Q_{CO}\rho_{CO})Q_{CO} - D_1\left(1 - \frac{D_2}{D_1}\right) = 0. \quad (29)$$

There are combined to give

$$\rho_{CO} = -\left(\frac{D_1 - D_2 - 2Q_{CO}}{D_1 - D_2 - 2Q_{CO}^2}\right). \quad (30)$$

Substitution of (30) into (28) gives

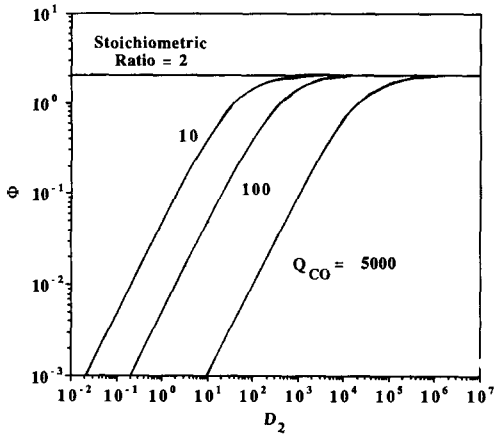

FIG. 12. Predicted dependence of the CO–oxygen bulk pressure ratio (Φ) resulting in extinction on D_2 for several values of $Q_{CO}(=K_{CO}p_{bCO})$. The asymptotic approach to the stoichiometric ratio (2) under conditions of severe transport limitations ($D_2 \to \infty$) is apparent.

$$D_2^2u^2 + D_2(1 - Q_{CO}^2 - 4Q_{CO})u + 4Q_{CO}^3 = 0, \quad (31)$$

where

$$u = \left(\frac{\nu}{\Phi} - 1\right) \quad \text{and} \quad \Phi = \frac{p_{bCO}}{p_{bO_2}}. \quad (32)$$

Equation (31) is quadratic in u. There are two roots, only one of which satisfies the assumption of severe transport limitations ($p_{CO} \to 0$). Figure 12 shows the dependence of Φ on D_2 for several values of Q_{CO}. As D_2 gets very large, the value of $u \to 0$. That is, $\Phi(=p_{bCO}/p_{bO_2}) \to \nu = 2$.

This analytical analysis demonstrates that for a simpler kinetic model extinction occurs at the stoichiometric point for a transport-limited reaction. Together with the simulations using the more realistic kinetic model, these results suggest that this is a general result independent of the details of the kinetic model, as long as the model predicts a rate maximum at an intermediate CO pressure.

Finally, Fig. 13 shows a close-up of maps A and B (from Fig. 12) in the vicinity of the lower temperature cusp. It is clear that an increase in limitations (A to C) moves the cusp to lower temperature and CO pressure. Also, the region of multiplicity expands significantly due primarily to a shift in the extinction branch to higher CO pressures. These trends are confirmed by the experimental temperature–CO pressure maps (Figs. 8 and 10). As mentioned earlier, the switch from helium to nitrogen reduces the external transport limitations. The only real inconsistency is the shift in the ignition branch to higher CO pressures during the switch from He to N_2. This experimental shift is larger than that predicted. Again, this reveals an effect of the diluent on the intrinsic kinetics.

CONCLUDING REMARKS

In this second of a two-part study the kinetics of Pt-catalyzed CO oxidation are simulated using two of the models developed in the first part. Our aim has been to discriminate between the models based on their robustness in predicting CO oxidation kinetics over a wide range of temperatures, gas compositions, and total pressures.

The first discrimination tests the models using experimental data obtained at UHV in which the rate is multivalued for a range of temperatures and gas compositions. A novel regression scheme provides an efficient

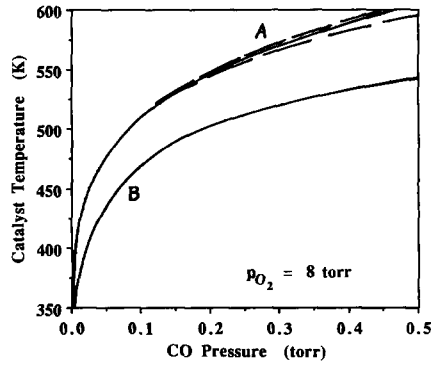

FIG. 13. Close-up of the low-temperature cusp in the temperature–CO pressure plane for cases A and B in Fig. 11.

check of a model based on the ability to simultaneously predict the location of singular and nonsingular points. This initial screening confirms whether or not a potential model can predict the intrinsic kinetic features observed in surface science studies. The second test checks the capability of a model to predict higher pressure behavior using the parameters estimated from the UHV data simulation. The final test is to check if high-pressure CO oxidation kinetics under conditions of external mass transport limitations can be simulated.

Both models II and III capably predict the basic kinetics and rate multiplicity features observed by Sung (*2*) for UHV CO oxidation on Pt(110). Models II and III give similar predictions for the UHV data, preventing a conclusive discrimination between the models at this level. Model IV is unable to simulate the data as well suggesting that the exclusion of vacant sites by adsorbed CO for additional CO adsorption may not be a viable mechanism. More likely are steps involving molecular oxygen; i.e., steps (4), (5), and (6) in models II and III. The simulations show that only in the CO inhibition regime does the coverage of molecular oxygen exceed that of atomic oxygen. The molecular oxygen coverage is several orders of magnitude less than the CO coverage. This may explain why direct experimental evidence for adsorbed molecular oxygen has been evasive and why its existence has been ignored in most previous models of CO oxidation. The comparable performance of models II and III suggests that either the ER reaction between CO and adsorbed oxygen or oxygen site exclusion are viable mechanisms for predicting first-order behavior at low CO/O_2 pressure ratios.

Model II and III simulations of intermediate pressure CO oxidation in the CO inhibition regime show quite good agreement with data for Pt(100) (Berlowitz *et al.* (*3*)) and polycrystalline Pt (Garske and Harold (*4*, *5*)). These simulations underscore the contention of Cant *et al.* (*9*) and Berlowitz *et al.* (*3*) that CO oxidation is structure insensitive in this regime. More importantly, the model II simulations demonstrate that the Eley–Rideal mechanism between CO and adsorbed oxygen should not be ignored as a potential reaction step, especially at intermediate and high pressure. Moreover, an Eley–Rideal reaction between oxygen and adsorbed CO is shown to explain the zero-order dependence on CO and low activation energy at low temperature observed in some studies.

Finally, a modified version of model II containing external mass transport resistance was used to simulate atmospheric pressure CO oxidation experiments. Rate multiplicity is shown to expand to a much larger range of conditions. The model predicts several experimentally observed trends, such as the upright cusp shape of the temperature–CO pressure bifurcation map for low CO/O_2 observed in many studies, and the transition in the extinction branch at the stoichiometric ratio observed in (*6*).

In this two-part study we have focused on the modeling of the much-studied Pt-catalyzed CO oxidation. Our approach has been to demand that potential kinetic models predict both the kinetic and multiplicity features. That the five models we have considered can all predict at least the qualitative experimental multiplicity features is evidence that prediction of the location of ignition and extinction points alone is not a sufficient discrimination tool. The basic kinetic features as well must be satisfied by a potential model. Satisfaction of both over a wide range of total pressure provides for sensitive discrimination between rival kinetic models. The fact that we cannot rule out either model II or III despite these stringent demands points to the complexity of CO oxidation. Nevertheless, extrapolation of a kinetic model using parameters estimated from a simulation of UHV data is a revealing way of bridging the gap between surface science and realistic operating pressures.

APPENDIX A: LIST OF NOTATION

D_1, D_2	parameters defined in Eq. (27)
E_i ($i = -1$, -2, 3, etc.)	activation energy of step i
f	oxygen site exclusion parameter
F_i ($i = 1, 2, 3$)	functions defined in Eqs. (18), (19), and (20)
ΔH_a	heat of adsorption
k_i ($i = 1, -1$, 2, -2, etc.)	rate constant of step i
k_{pi} (i = CO, O_2)	mass transfer coefficient for species i
k_r	surface reaction rate constant for simple model (Eq. (22))
K_i (i = CO, O_2)	adsorption equilibrium constant for species i
M	molecular weight
M	parameter sensitivity matrix defined in Appendix B
N	number of experiments
N_{ns}, N_s	number of nonsingular and number of singular points
N_p, N_r	number of parameters and number of responses
p	pressure
p	vector of parameters
q	response
Q	volumetric flowrate
Q_i	dimensionless adsorption equilibrium constant for species i
r	dimensionless rate
r	residual vector defined in Appendix B
R	Universal gas constant
S_i	sticking probability of species i
S_c	surface area of catalyst
T	temperature
y	dimensionless temperature

Greek Symbols

Φ	parameter defined in (32)
λ	stepping parameter defined in Appendix B
ν	stoichiometric coefficient
Ω	objective function defined by (5)
Ψ	parameter given by $k_{10}p_{O_2}/k_3$
ρ_i	reduced pressure of species i (Eq. (13))
σ	reciprocal of variance
θ	surface coverage

Subscripts

a	adsorption
b	bulk
c	catalyst
CO	carbon monoxide
ns	nonsingular
O, O_2	atomic and molecular oxygen
p	parameter
r	reference or response
s	singular
un	unknown
v	vacant
w	wire

Superscripts

o	denoting preexponential factor
*	optional parameter vector

APPENDIX B

Parameter Estimation Scheme for Simulating UHV CO Oxidation Data of Sung (2)

The algorithm for estimating the set of parameters from a fit of singular and nonsin-

gular data is a modified multiresponse Levenberg–Marquardt optimization (*19*). Given an initial guess for the parameters $\mathbf{p}_{un}$ the aim is to minimize the objective function

$$\Omega = \sum_{k=1}^{N_r}\sum_{l=1}^{N_r}\sigma_{kl}\sum_{j=1}^{N}(q-\hat{q})_{kj}(q-\hat{q})_{lj} \quad \text{(B1)}$$

by proper adjustment of the parameters. The solution $\mathbf{p} = \mathbf{p}_{un}^{*}$ satisfies

$$\Omega \xrightarrow{\mathbf{p}_{un}=\mathbf{p}_{un}^{*}} \min. \quad \text{(B2)}$$

N_r in Eq. (B1) is the total number of responses for each experiment, N is the number of experiments, and q and $\hat{q}$ are the predicted and measured responses, respectively. The term σ_{kl} is the (kl)th element of the inverted error variance–covariance matrix.

For our application, the N experiments are divided into N_s singular points measurements and N_{ns} nonsingular point measurements. The former involves two responses, the CO pressure and rate; the latter involves a single response, the rate. The two-responses ($N_r = 2$) form of (B1) was used by letting $p_{CO} = \hat{p}_{CO}$ for the N_{ns} experiments. In addition, we assumed $\sigma_{kl} = 0$ $(k \neq l)$.

The parameter estimates are updated by the formula

$$\mathbf{p}_{un}^{i+1} = \mathbf{p}_{un}^{i} + \Delta\mathbf{p}_{un}^{i} \quad \text{(B3)}$$

$$\Delta\mathbf{p}_{un}^{i} = \sum_{k=1}^{N_r}\sum_{l=1}^{N_r}(\sigma_{kl}\mathbf{M}_{ki}^{T}\mathbf{M}_{li} + \lambda\mathbf{I})^{-1} \sum_{k=1}^{N_r}\sum_{l=1}^{N_r}(\sigma_{kl}\mathbf{M}_{ki}^{T}\mathbf{r}_{li}), \quad \text{(B4)}$$

where $\mathbf{r}_{li}$ is the N-dimensional residual vector given by

$$\{\mathbf{r}_u\}_{li} = (q_{lu} - \hat{q}_{lu})_{\mathbf{p}_{un}=\mathbf{p}_{un}^{i}} \quad l = 1, \ldots, N_r;\ u = 1, \ldots, N. \quad \text{(B5)}$$

Again note that $\{r_u\}_{li} = 0$ for $i =$ nonsingular experiment. $\mathbf{M}_{ki}$ is the $N \times N_p$ (number of parameters in $\mathbf{p}_{un}$) sensitivity matrix given by

$$\{\mathbf{M}_{uv}\}_{ki} = \left(\frac{\partial q_{ku}}{\partial p_v}\right)_{\mathbf{p}_{un}=\mathbf{p}_{un}^{i}} \quad K = 1, \ldots, N_r;\ v = 1, \ldots, N_p;\ u = 1, \ldots, N. \quad \text{(B6)}$$

The elements of $\mathbf{M}$ are determined by numerical differentiation.

ACKNOWLEDGMENTS

The support of grants from ACS-PRF (no. 18322-G5) and DOE Basic Energy Sciences (no. DE-FG 02-87ER13772) is gratefully acknowledged.

REFERENCES

1. Harold, M. P., and Garske, M. E., *J. Catal.* **127,** 524 (1990).
2. Sung, B. P., Sc. dissertation, Massachusetts Institute of Technology (1981).
3. Berlowitz, P. J., Peden, C. H. F., and Goodman, D. W., *J.Phys. Chem.* **92,** 5213 (1988).
4. Garske, M. E., and Harold, M. P., "N. A. Catalysis Soc. Meeting, Dearborn, MI (1989)."
5. Garske, M. E., and Harold, M. P., to be submitted for publication (1991).
6. Kaul, D. J., Sant, R., and Wolf, E. E., *Chem. Eng. Sci.* **42,** 1399 (1987).
7. Engel, T., and Ertl, G., *Adv. Catal.* **28,** 1 (1979); *J. Chem. Phys.* **69,** 1267 (1978).
8. Razon, L. F., and Schmitz, R. A., *Catal. Rev. Sci. Eng.* **28,** 89 (1986).
9. Cant, N. W., Hicks, P.C., and Lennon, B. S., *J. Catal.* **54,** 372 (1978).
10. Golchet, A., and White, J. M., *J. Catal.* **53,** 266 (1978).
11. Taylor, J. L., Ibbotson, D. E., and Weinberg, W. H., *J. Catal.* **62,** 1 (1980).
12. Herz, R. K., and Marin, S. P., *J. Catal.* **65,** 281 (1980).
13. Ertl, G., Norton, P. R., and Rüstig, J., *Phys. Rev. Lett.* **49,** 177 (1982).
14. Cox, M. P., Ertl, G., and Imbihl, R., *Phys. Rev. Lett.* **54,** 1725 (1985).
15. Imbihl, R., Cox, M. P., Ertl, G., Muller, H., and Brenig, W., *J. Chem. Phys.* **83,** 1578 (1985).
16. Möller, P., Wetzl, K., Eiswirth, M., and Ertl, G., *J. Chem. Phys.* **85,** 5328 (1986).
17. Harold, M. P., and Luss, D., *Ind. Eng. Chem. Res.* **26,** 2099 (1987).
18. Garske, M. E., Ph.D. dissertation, University of Massachusetts (1991).
19. Froment, G. F., and Hosten, L., *in "Catalysis*

Science and Technology" (J. R. Anderson and M. Boudart, Eds.), Vol. 6, p. 97. Springer-Verlag, New York (1984).
20. Eisworth, M., and Ertl, G., *Surf. Sci.* **177,** 90 (1986).
21. Eisworth, M., Krischer, K., and Ertl, G., *Surf. Sci.* **202,** 565 (1988).
22. McCabe, R. W., and Schmidt, L. D., *Surf. Sci.* **66,** 101 (1977).
23. Conrad, H., Ertl, G., and Kuppers, J., *Surf. Sci.* **76,** 323 (1978).
24. Langmuir, I., *Trans. Faraday Soc.* **17,** 621 (1921–1922).
25. Heyne, H., and Tompkins, F. C., *Proc. R. Soc. London Ser. A* **292,** 460 (1966).
26. Nicholas, D. M., and Shah, Y. T., *Ind. Eng. Prod. Res. Dev.* **15,** 35 (1976).
27. Chakrabarty, T., Hudgins, R. R., and Silveston, P. L., *J. Catal.* **77,** 527 (1982).
28. Ceyer, S., *Science*, 133 July, (1990).
29. Haaland, D. M., and Williams, J. L., *J. Catal.* **76,** 450 (1982).